A Novel Robust Dead-Beat Structure for Double Vector Model Predictive Control in Three-Level Inverter fed PMSM Drives

Zhenyao Sun, Junkai Wen, Xin Yuan, *Senior Member, IEEE*, Guangtong Ma, *Member, IEEE*, Shuangxia Niu, *Senior Member, IEEE* and K.T. Chau, *Fellow, IEEE*

[1]***Abstract*- Model predictive control (MPC) has recently been considered in permanent magnet synchronous motor (PMSM) drives due to its rapid dynamics and simple structure. However, conventional MPC utilizes only a single voltage vector per control cycle, and the prediction model relies heavily on the motor parameters. Hence, substantial current ripples and poor disturbance rejection have largely limited its adaptability to a variety of environment conditions. This paper presents a novel double vector MPC (DV-MPC) scheme for three-level inverter fed PMSM drives. To reduce the computational complexity of DV-MPC, the cost function is derived with the reference voltage by employing the dead-beat approach, and the inverter's neutral point potential is balanced using the complementary small voltage vectors. The dead-beat voltage prediction model is further enhanced by incorporating an active damping framework and an extra coefficient to enhance the robustness against parameter variations and disturbance rejection. Moreover, a robust current predictor is designed for the delay compensation. The proposed method is straightforward to implement, and achieves strong disturbance rejection and parameter robustness with a fast dynamic response. Experimental results demonstrate the effectiveness of the proposed method.**

***Index Terms*- AC motor drive, double vector, model predictive control (MPC), robustness, three-level inverter.**

I. INTRODUCTION

Motivated by the challenge to attain carbon neutrality and net-zero emissions in the civil aviation sector by 2050, industrial and academic researchers' interest has gradually shifted from the conventional internal combustion engine to the full electric aircraft design [1], [2]. Owing to advantages in higher efficiency and lower harmonic distortion, three-level inverters have gained prominence in high-power AC machine drives, such as electrical propulsion systems for aviation [3], [4]. To meet the demands for fast dynamic response and high steady-state precision, various current controllers have been developed for electric propulsion systems. The most commonly used methods during the last few years include the hysteresis control, proportional integral (PI) control, and model predictive control (MPC) [5].

Hysteresis control achieves rapid dynamic response, inherent robustness, and straightforward implementation [6], [7]. Nevertheless, the variable switching frequency and significant current ripple of hysteresis control render it unsuitable for precision-demanding electrical propulsion applications. The PI current controller is commonly employed with the field-oriented control architecture within synchronous reference frames, which typically requires an external modulation stage. While its parameters can be conveniently designed using the internal model control (IMC) principle [8], the controller struggles to address system nonlinearities and disturbances. These shortcomings lead to compromised dynamic performance under high-bandwidth conditions, manifesting as current overshoot and oscillations [9], [10], which may negatively impact electric propulsion systems with high dynamic response requirements.

Recently, model predictive control (MPC) has been developed remarkably and is shown tremendous potential in high-power motor drive applications, due to its multi-objective and constraints handling ability [11], [12]. Based on the established model, MPC can predict the future system states and outputs, where the two branches, i.e. the continuous control set MPC (CCS-MPC) and finite control set MPC (FCS-MPC), have been derived subjecting to type of the output [13]. The FCS-MPC explicitly accounts for the inverter's nonlinear voltage outputs, enabling direct switching state calculation without external modulator, which thereby presents superior dynamic response [14], [15].

Thanks to the intuitive design and simple implementation, FCS-MPC becomes more favored than the CCS-MPC, and numerous studies working for FCS-MPC with three-level inverter drive applications can be found in recent literatures [16]–[18]. Nevertheless, FCS-MPC demands extremely high sampling frequency for low current harmonics, which is not applicable for all microprocessors [19]. Unless operating with a very low inverter switching frequency, the steady state

This work was supported in part by the Research Grant Council of the Hong Kong Government under Projects PolyU 152109/20E and in part by RGC Collaborative Research Fund under Grant C1052-21G. *(Zhenyao Sun and Junkai Wen contributed equally to this work.) (Corresponding author: Shuangxia Niu)*

Zhenyao Sun, Junkai Wen, Shuangxia Niu, and K. T. Chau are with the Department of Electrical and Electronic Engineering, The Hong Kong Polytechnic University, Hong Kong 999077, China (e-mail: zhenyao.sun@polyu.edu.hk; 22116996r@connect.polyu.hk; eesxniu@polyu.edu.hk; k.t.chau@polyu.edu.hk)

Xin Yuan is with the School of Engineering, University of Aberdeen, AB24 3UF Aberdeen, U.K. (e-mail: xin.yuan@abdn.ac.uk).

Guangtong Ma is with the School of Electrical Engineering, and also with the State Key Laboratory of Rail Transit Vehicle System, Southwest Jiaotong University, Chengdu 610031, China (e-mail: gtma@swjtu.edu.cn).

performance of FCS-MPC can be inferior than the field-oriented control with PI current controller for [20]. To solve this issue, the concept that include multiple voltage vectors into one control cycle was introduced [21]. In this method, more than one voltage vector will be selected with the defined cost function, and the dwell time for each vector is calculated to minimize either the current [22]–[24] or the torque errors [25]–[26]. Furthermore, the calculation of voltage vectors was simplified based on the reference voltage cost function, using the dead-beat approach [27]. This simplicity method can prominently reduce the computational costs in three-level inverters [28]–[30].

However, since the accuracy of dwell time calculation strongly relies on the prediction model, multi-vector MPC becomes highly sensitive to parameter variations in the permanent magnet synchronous motor (PMSM) model [31]. In addition, the unmodeled external disturbance may constantly occur with different operation conditions regarding the various environment, which can further deteriorate the control performance. Only the feedback error regulation cannot change the low stiffness of the model plant and damping characteristic, resulting in insufficient external disturbance rejection ability.

Due to the simple structure, the active damping method is proposed for the current loop to improve the disturbance rejection [32], [33]. However, the active damping is mostly reported in FOC frameworks, while few researches investigate the application with MPC architectures. The MPC with extended state observer has been widely adopted to compensate for model uncertainties [34]–[36]. This approach treats external disturbances and parameter variations as a lumped disturbance, which can be further estimated by various of observers. However, a relative higher bandwidth or a higher observer order are required to enhance the estimation accuracy and disturbance rejection ability. As a result, all types of the system noises will be inevitably amplified [37]. Hence, MPC with observer may not be universal for all kinds of drive applications, especially for the low noise application.

In this paper, the active damping framework and a coefficient for additional control degree of freedom are firstly introduced to DV-MPC, retaining the fast dynamic response and significantly improve the disturbance rejection capability. The key contributions can be summarized as follows:

1) A simple double vector MPC is developed for a three-level inverter fed PMSM drive. The computational complexity can be largely decreased by a voltage-based cost function and simplified dwell time derivation. Furthermore, the switching sequence that considers the neutral point potential balance is derived, enabling straightforward implementation.

2) In order to improve the disturbance rejection, anti-parameter mismatch ability, and streamline the design process simultaneously, the effects of parameter mismatch on the MPC performance are analyzed in detail. An active damping framework and a coefficient for additional control degree of freedom are incorporated into the prediction model in DV-MPC for the first time. The selection and impact of these three coefficients are comprehensively studied, demonstrating that the proposed approach achieves not only strong robustness and disturbance rejection but also deadbeat responses.

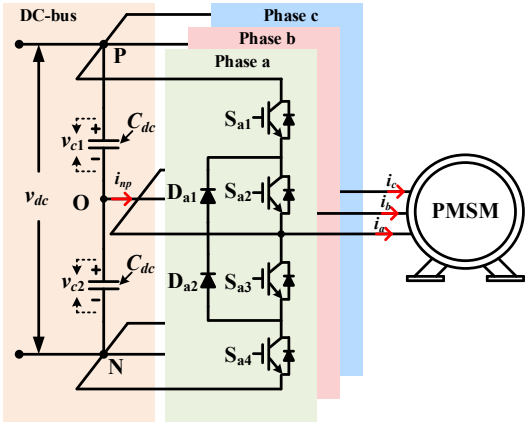

Fig. 1. Circuit topology of a 3-level inverter NPC inverter fed PMSM.

3) A simple current estimator is introduced to compensate for controller delays. Unlike the MPC with observer, the current estimator offers a new degree of freedom for the tradeoff between dynamic response and noise components, which does not affect the disturbance rejection performance.

4) The proposed method is experimentally validated on the NPC inverter-fed PMSM drive platform, and its performance is comprehensively compared with conventional methods.

II. System Modeling and Conventional FCS-MPC

A. Model of NPC Inverter and PMSM

Consider a simplified circuit topology with a PMSM fed by 3-level neutral point clamped (NPC) inverter, as the one illustrated in Fig. 1. In this figure, v_{dc} denotes the DC-link voltage; v_{c1} and v_{c2} are the voltage for upper and lower capacitor, respectively. i_{np} denotes the neutral point current. i_a, i_b, and i_c are the three phase currents of the PMSM. The red arrows in Fig. 1 indicate the positive current direction. The switch position of the NPC inverter can be defined as

$$\boldsymbol{u} = \begin{bmatrix} u_a & u_b & u_c \end{bmatrix}^T, \tag{1}$$

where $\boldsymbol{u}$ can be seen as the voltage vector in the stationary reference frame. Each element u_x $\{u_x \in (-1, 0, 1)\}$ in the voltage vector represents the normalized output voltage of x $\{x \in (a, b, c)\}$ phase, corresponding to the original output phase voltage ($-v_{dc}/2$, 0, $v_{dc}/2$). Accordingly, 27 alternative voltage vectors are derived from the 3-level NPC inverter.

Since that the PMSM is normally controlled in the rotational dq frame, the inverter's output voltage vector can be transformed into the dq-axis voltage by

$$\boldsymbol{u}_{dq} = \frac{1}{2} v_{dc} \boldsymbol{K} \boldsymbol{u}, \tag{2}$$

$$\boldsymbol{K} = \frac{2}{3} \begin{bmatrix} \cos\theta_r & \cos\left(\theta_r - \frac{2}{3}\pi\right) & \cos\left(\theta_r + \frac{2}{3}\pi\right) \\ -\sin\theta_r & -\sin\left(\theta_r - \frac{2}{3}\pi\right) & -\sin\left(\theta_r + \frac{2}{3}\pi\right) \end{bmatrix}, \tag{3}$$

where $\boldsymbol{u}_{dq}=[u_d\ u_q]^T$ represents the inverter output voltage, and u_d and u_q are the corresponding dq-axis voltages. $\boldsymbol{K}$ denotes the matrix that transforms the variables in the stationary frame into the rotational frame. θ_r is the electrical angle for PMSM.

The neutral point (NP) potential of NPC inverter should be modeled for its balancing. Firstly, the NP potential denoted by v_{np} can be obtained based on the capacitor voltage, yielding

$$v_{np}=\frac{1}{2}\left(v_{c2}-v_{c1}\right), \tag{4}$$

Then, according to the phase current i_x $\{x\in(a, b, c)\}$, and the normalized phase voltage u_x, the dynamic of NP current can be derived as

$$i_n=\sum_{x\in(a,b,c)}\left(-i_x\left|u_x\right|\right). \tag{5}$$

The relationship between NP potential and NP current is given by

$$\frac{dv_n}{dt}=-\frac{1}{2C_{dc}}i_n, \tag{6}$$

where C_{dc} represents the capacitance of each capacitor. Based on (5) and (6), we have

$$\frac{dv_n}{dt}=\frac{1}{2C_{dc}}\sum_{x\in(a,b,c)}\left(i_x\left|u_x\right|\right), \tag{7}$$

The PMSM model based on the rotational dq synchronous frame can be simplified by ignoring the inverter nonlinearity, cogging torques, etc. Hence, the ideal voltage equation of the PMSM can be expressed as

$$\dot{\boldsymbol{i}}_{dq}=\boldsymbol{A}\boldsymbol{i}_{dq}+\boldsymbol{B}\boldsymbol{u}_{dq}+\boldsymbol{D}, \tag{8}$$

where $\boldsymbol{i}_{dq}=[i_d\ i_q]^T$ represents the stator current in the dq synchronous frame. The matrices in (9) are given by

$$\boldsymbol{A}=\begin{bmatrix}-\frac{R_s}{L_d} & \frac{L_q\omega_r}{L_d}\\ -\frac{L_d\omega_r}{L_q} & -\frac{R_s}{L_q}\end{bmatrix},\ \boldsymbol{B}=\begin{bmatrix}\frac{1}{L_d} & 0\\ 0 & \frac{1}{L_q}\end{bmatrix},\ \boldsymbol{D}=\begin{bmatrix}0\\ -\frac{\psi_f\omega_r}{L_q}\end{bmatrix}. \tag{9}$$

where i_d and i_q are the stator currents; R_s is the stator winding resistance; L_d and L_q are the stator inductances; ψ_f is the flux linkage of the permanent magnets; and ω_r represents the rotor electrical angular speed.

B. MPC With Voltage-based Cost Function

Based on (8), the dq-axis current at next time instant is normally predicted with the forward Euler discretization method, yielding

$$\boldsymbol{i}_{dq}\left(k+1\right)=\left(\boldsymbol{I}+\boldsymbol{A}T_s\right)\boldsymbol{i}_{dq}\left(k\right)+\boldsymbol{B}T_s\boldsymbol{u}_{dq}\left(k\right)+\boldsymbol{D}T_s, \tag{10}$$

where T_s denotes the sampling period, and k indicates the present time instant of the controller. Due to the exhaustive searching of FCS-MPC, (10) have be calculated by utmost 27 times (if no switch constraint is implemented), leading to a high computational expense. Hence, the reference current tracking can be normally converted into the reference voltage tracking by adopting the dead-beat MPC approach, which avoids the current prediction during the iteration, and can be equivalent to the current tracking form. The calculation is given as

$$\boldsymbol{u}^*_{dq}\left(k+1\right)=\boldsymbol{B}^{-1}T_s^{-1}\left[\boldsymbol{i}^*_{dq}\left(k+1\right)-\left(\boldsymbol{I}+\boldsymbol{A}T_s\right)\boldsymbol{i}_{dq}\left(k+1\right)-\boldsymbol{D}T_s\right], \tag{11}$$

where the superscript * denotes the variable with a reference value. In (11), the measured current is compensated by one sampling period considering the controller's execution time delay. Hence, the current at $(k+1)^{\text{th}}$ instant is calculated by (10) using the voltage at last $(k)^{\text{th}}$ instant.

Based on (7), NP potential of the inverter can be predicted in the discrete formulation as

$$v_{np}\left(k+1\right)=v_{np}\left(k\right)+\frac{T_s}{2C_{dc}}\sum_{x\in(a,b,c)}\left(i_x\left|u_x\right|\right), \tag{12}$$

The number of switch transitions is defined to penalize the average switching frequency. For each candidate vector from the available set, the number of switch transitions from its $(k)^{\text{th}}$ state to $(k+1)^{\text{th}}$ state for the three phases is obtained by

$$\Delta u\left(k+1\right)=\left\|\boldsymbol{u}\left(k+1\right)-\boldsymbol{u}\left(k\right)\right\|, \tag{13}$$

where Δu represents the number of voltage level changes for the new vector to be enumerated.

The cost function can be constructed with three control objectives: reference tracking, NP voltage balance and average switching frequency penalization, which is expressed as

$$J=\left\|\boldsymbol{u}^*_{dq}\left(k+1\right)\text{-}\boldsymbol{u}_{dq}\left(k+1\right)\right\|_2+\lambda_1\left\|v_{np}\left(k+1\right)\right\|+\lambda_2\left\|\Delta u\left(k+1\right)\right\|, \tag{14}$$

where λ_1 and λ_2 represent the weight factors, and is to adjust the priority of their corresponding control objectives.

The conventional MPC method discussed above suffers from two major limitations that adversely impact the PMSM control performance. First, only a single voltage vector is applied during each sampling period, which is insufficient to effectively track the reference with low errors. This drawback becomes even pronounced with the high average switching frequency operation (i.e., when λ_2 is too small). Second, the prediction model exhibits high sensitivity to parameter variations and external disturbances. The model mismatch in (10) and (11) can significantly degrade the control performance. To address the aforementioned two challenges, a simple DV-MPC with and enhanced dead-beat structure is proposed in the following section.

III. Proposed Method

A. Double Vector MPC

1) Voltage vector selection: The optimal voltage vectors are determined through the plain reference tracking cost function without weight factors, which can be expressed as follow:

$$J_2=\left\|\boldsymbol{u}^*_{dq}\left(k+1\right)-\boldsymbol{u}_{dq}\left(k+1\right)\right\|_2, \tag{15}$$

where J_2 is norm of the difference between reference voltage and candidate voltage, indicating the geometric distance between these two variables.

The three-level NPC inverter can produce 19 kind of voltage vectors regardless of the redundant zero and small voltage vectors. By minimizing the cost function value with the 19 candidate voltage vectors, the optimal vector V_{opt1} and the second optimal vector V_{opt2} can be determined.

Fig. 2 gives an example of the optimal voltage vector selection principle. V1 is the zero voltage vector; V2-V7 are the small voltage vectors, and the redundant vector with the same voltage output is marked as P and N; V8-V13 are the medium voltage vectors; V14-V19 are the large voltage vectors. The reference voltage $\boldsymbol{u}_{dq}^{*}$ will locate in either of the triangular sector, and each sector can be further divided into three zones by the green dashed lines. Based on the smallest distance principle, the value calculated by the cost function in (15) equals to the length of red dashed line in Fig. 2. In this case, V2 is the nearest voltage vector to the reference, and V8 is the second nearest one. According to Fig. 2, the selected two vectors can always be adjacent to each other, and both vectors are the active vectors that can be either zero or non-zero vector.

2) Duty cycle calculation: The duty cycle for the two optimal voltage vector has the following relationship:

$$d_1 + d_2 = 1, \tag{16}$$

where d_1, d_2 are the duty cycle of the optimal vector V_{opt1} V_{opt2}, respectively.

The synthesized voltage can move along the line between the selected two vectors by adjusting their duty cycle. Thus, the synthesized voltage $\boldsymbol{u}_{dq}^{syn}$ can be expressed as

$$\boldsymbol{u}_{dq}^{syn}(k+1) = d_1(k+1)\boldsymbol{u}_{dq1}(k+1) + d_2(k+1)\boldsymbol{u}_{dq2}(k+1), \tag{17}$$

where $\boldsymbol{u}_{dq1}$ and $\boldsymbol{u}_{dq2}$ are the dq voltage of the selected optimal voltage vectors.

The theoretically optimal synthesized voltage vector should have the smallest distance to the reference voltage $\boldsymbol{u}_{dq}^{*}$. By substituting (16), (17) into (15), the optimal duty cycle can be derived with $\partial J_2/\partial T_1 = 0$, yielding

$$d_1(k+1) = \frac{\left(u_d^*(k+1) - u_{d2}(k+1)\right)\left(u_{d1}(k+1) - u_{d2}(k+1)\right)}{\left\|\boldsymbol{u}_{dq1}(k+1) - \boldsymbol{u}_{dq2}(k+1)\right\|_2^2} + \frac{\left(u_q^*(k+1) - u_{q2}(k+1)\right)\left(u_{q1}(k+1) - u_{q2}(k+1)\right)}{\left\|\boldsymbol{u}_{dq1}(k+1) - \boldsymbol{u}_{dq2}(k+1)\right\|_2^2}. \tag{18}$$

However, the calculation of the theoretically optimal dwell time is too complicated and computationally expensive. To simplify the calculation, the optimal duty cycle for the two voltage vectors can be calculated based on the value of the cost function without sacrificing too much accuracy, which derives

$$\begin{cases} d_1 = \dfrac{J_2^{opt2}}{J_2^{opt1} + J_2^{opt2}} \\ d_2 = \dfrac{J_2^{opt1}}{J_2^{opt1} + J_2^{opt2}}, \end{cases} \tag{19}$$

where J_2^{opt1} and J_2^{opt2} are the value of the two selected optimal voltage vectors, as showing in Fig. 2.

3) Switching sequence considering NP potential balance: The NP potential can be balanced based on the redundant small voltage vector pairs, which share the same voltage output with opposite NP current direction. The P type vectors can decrease the NP potential v_{np}, while the N type vectors will increase v_{np}. The type of the selected small voltage vector can be determined based on the sign of NP potential, and the switching sequence

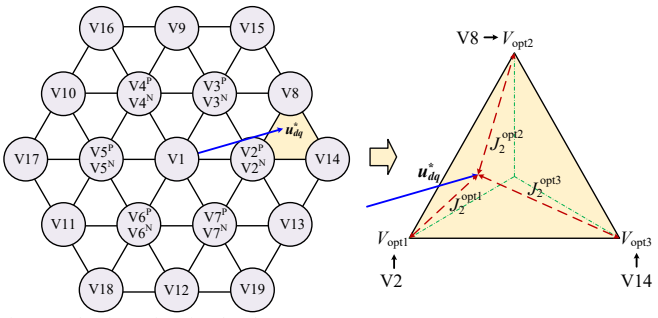

Fig. 2. Selection of optimal voltage vectors.

TABLE I. Pulse generation with different voltage vectors

V_{opt1} for phase x $\{x\in(a, b, c)\}$	V_{opt2} for phase x $\{x\in(a, b, c)\}$	Duty cycle of S_{x1}	Duty cycle of S_{x2}
1	1	T_s	T_s
1	0	T_1	T_s
0	1	T_2	T_s
0	0	0	T_s
0	-1	0	T_1
-1	0	0	T_2
-1	-1	0	0

will be adjusted accordingly. The control algorithm can be described as follows:

Step 1: Identify the two selected optimal voltage vectors. If a small voltage vector is chosen, the sign of v_{np} will be determined. A P-type small vector will be utilized if v_{np} is negative; otherwise, an N-type small vector will be adopted.

Step 2: Determine the voltage levels of the two voltage vectors for each phase and assign the corresponding duty cycles to the switches. TABLE I summarizes the duty cycle assignment method, where seven cases are identified for each phase.

B. Robust Dead-Beat Structure with Active Damping

Traditionally, the transfer function of PMSM and the deadbeat voltage prediction model can be derived based on (10) and (11), which is given as:

$$\begin{cases} G_{pd}(z) = \dfrac{\boldsymbol{i}_{dq}(z)}{\boldsymbol{u}_{dq}(z)} = \dfrac{\boldsymbol{B}T_s}{z-1} \\ G_{cd}(z) = \dfrac{\alpha T_s}{z-1} G_{pd}^{-1}(z) = \dfrac{\alpha}{\boldsymbol{B}} = \dfrac{1}{\boldsymbol{B}T_s}, \end{cases} \tag{20}$$

where $G_{pd}(z)$ is the transfer function of the plant and $G_{cd}(z)$ is the controller's transfer function with the deadbeat approach. Herein, α is the bandwidth and is fixed as T_s^{-1}, giving the rapid dynamic response for the deadbeat voltage prediction.

However, due to the PMSM model reducing to a pure integrator in this configuration, the disturbance rejection capability is significantly weakened, and the system performance becomes highly sensitive to parameter variations. Generally, the look-up-table, online parameter identification methods, and the extended disturbance observers (ESO) can be applied to improve the disturbance rejection and overcome the parameter mismatches. However, all the above methods require a complex design process, and the initial inductance parameter meters in controllers are still needed in the ESO [35].

In this case, an enhanced structure for voltage prediction including a simple coefficient with active damping framework is built. The design and analysis of the proposed structure is shown as follows: First, considering the one step delay caused by the execution time, the discrete transfer function of the PMSM model (8) can be presented as follows:

$$G_{p1}(z)=\frac{\boldsymbol{i}_{dq}(z)}{\boldsymbol{u}_{dq}(z)}=\frac{\boldsymbol{B}T_s}{z\left[(z-1)\boldsymbol{I}-\boldsymbol{A}T_s\right]}. \tag{21}$$

Based on (21), a current controller can be simply designed through the IMC principle as follows:

$$G_{c1}(z)=\frac{\alpha T_s}{z(z-1)}G_{p1}^{-1}(z), \tag{22}$$

From equations (10) and (11), it is evident that the accuracy of FCS-MPC is highly sensitive to parameter mismatches. Thereafter, in order to quantify the prediction error due to parameter variation and introduce the proposed framework, the PMSM model under parameter mismatches is derived as:

$$\boldsymbol{u}_{dq}=\boldsymbol{B}_c^{-1}\dot{\boldsymbol{i}}_{dq}-\boldsymbol{B}_c^{-1}\boldsymbol{A}_c\boldsymbol{i}_{dq}-\boldsymbol{B}_c^{-1}\boldsymbol{D}_c+\boldsymbol{E}_{dq}, \tag{23}$$

$$\boldsymbol{E}_{dq}=\left(\boldsymbol{B}^{-1}-\boldsymbol{B}_c^{-1}\right)\dot{\boldsymbol{i}}_{dq}-\left(\boldsymbol{B}^{-1}\boldsymbol{A}-\boldsymbol{B}_c^{-1}\boldsymbol{A}_c\right)\boldsymbol{i}_{dq}-\left(\boldsymbol{B}^{-1}\boldsymbol{D}_c-\boldsymbol{B}_c^{-1}\boldsymbol{D}\right), \tag{24}$$

where $\boldsymbol{A}_c$, $\boldsymbol{B}_c$, and $\boldsymbol{D}_c$ are the matrices adopted in the controller; $\boldsymbol{E}_{dq}$ denotes the distortion voltage caused by the parameter mismatch. It can be observed that parameter mismatches will introduce a differential term with high frequency component. The high-frequency component will amplify disturbances and cannot be suppressed effectively.

In this case, in order to suppress all the disturbance caused by the parameter mismatch, a feedback term $\boldsymbol{\Xi}=R_s\boldsymbol{I}$ and the parameters δ are developed to reconstruct the PMSM model virtually to suppress the parameter mismatch in FCS-MPC. The command tracking closed-loop transfer function can be derived as follows:

$$\begin{aligned}G_{cl}(z)&=\frac{\boldsymbol{i}_{dq}(z)}{\boldsymbol{i}_{dq}^{*}(z)}=\frac{G_{c1}(z)G_{p1}(z)}{1+zG_{c1}(z)G_{p1}(z)}\\&=\frac{\alpha T_s\underbrace{\frac{\boldsymbol{B}}{\boldsymbol{B}_c}}_{Term1}\underbrace{\frac{\left[(z-1)\boldsymbol{I}-\boldsymbol{A}_cT_s\right]}{\left[(z-1)\boldsymbol{I}-\boldsymbol{A}T_s\right]}}_{Term2}}{z(z-1+\alpha T_s\underbrace{\frac{\boldsymbol{B}}{\boldsymbol{B}_c}}_{Term1}\underbrace{\frac{\left[(z-1)\boldsymbol{I}-\boldsymbol{A}_cT_s\right]}{\left[(z-1)\boldsymbol{I}-\boldsymbol{A}T_s\right]}}_{Term2})}.\end{aligned} \tag{25}$$

It can be seen from (25) that Term1 and Term2 cannot be effectively eliminated when the parameter mismatch occurs, in which Term1 relates to the inductance and Term2 is influenced by resistance. Motivated by this fact, the parameter δ is designed to suppress the parameter mismatch in term1, i.e., δ equal to the reciprocal of term1, $\delta=B_cB^{-1}$.

In matrix A_c and A of Term2, the value of L_{qc}/L_{dc} and L_d/L_q is expected to be constant. For a surface-mounted PMSM, we can assume $L_d/L_q=L_{qc}/L_{dc}=1$. Therefore, it is reasonable to neglect the distortion of cross-coupling terms $\omega_rL_qL_d^{-1}$ and $\omega_rL_dL_q^{-1}$ due to parameter mismatches. However, the resistive drop terms $-R_sL_d^{-1}$ and $-R_sL_q^{-1}$ cannot be neglected when the parameter mismatch occurs. Therefore, the feedback term $\boldsymbol{\Xi}=R_s\boldsymbol{I}$ can be introduced into the controller to eliminate this term, i.e., decoupling the effects of the resistance value R_s. In this manner, the PMSM's transfer function $G_{p2}(z)$ and the corresponding controller transfer function $G_{c2}(z)$ can be reconstructed with

$$\begin{cases}G_{p2}(z)=\dfrac{\boldsymbol{i}_{dq}(z)}{\boldsymbol{u}_{dq}(z)}=\dfrac{\boldsymbol{B}T_s}{z\left[(z-1)\boldsymbol{I}-\boldsymbol{M}T_s\right]}\\G_{c2}(z)=\delta\dfrac{\alpha T_s}{z(z-1)}G_{p2}^{-1}(z)\end{cases}, \tag{26}$$

where $\boldsymbol{M}=\begin{bmatrix}0 & \dfrac{L_q\omega_r}{L_d}\\ -\dfrac{L_d\omega_r}{L_q} & 0\end{bmatrix}$.

The closed loop transfer function of (26) can be derived as:

$$\begin{aligned}G_{cl1}(z)&=\frac{G_{p2}(z)G_{c2}(z)}{1+zG_{p2}(z)G_{c2}(z)}\\&=\delta\boldsymbol{B}\boldsymbol{B}_c^{-1}\frac{\alpha T_s}{z\left[z-1+\alpha T_s\delta\boldsymbol{B}\boldsymbol{B}_c^{-1}\right]}.\end{aligned} \tag{27}$$

Based on (27), the closed loop transfer function can be rewritten as $G_{cl1}(z)=z^{-2}$, when the deadbeat prediction approach with $\alpha=T_s^{-1}$ is applied. It can be seen that there are two control cycles between the reference current and the actual current. Nevertheless, when parameters mismatch occurs, i.e., $\boldsymbol{B}\neq\boldsymbol{B}_c$. δ should eliminate the distortion induced by the inconsistency between $\boldsymbol{B}$ and $\boldsymbol{B}_c$, suppressing the effects due to parameters mismatch and maintaining the deadbeat responses.

To further enhance the disturbance rejection ability with the dead-beat voltage prediction, the transfer function of disturbance to the current responses should be analyzed. Hence, the disturbance rejection transfer function can be derived by

$$\begin{aligned}G_{d1}(z)&=\frac{G_{p2}(z)}{1+zG_{p2}(z)G_{c2}(z)}\\&=\frac{\boldsymbol{B}T_s(z-1)}{z\left[(z-1)\boldsymbol{I}-\boldsymbol{M}T_s\right](z-1+\alpha T_s)}.\end{aligned} \tag{28}$$

It can be seen from (28) that $G_{d1}(z)$ provides a peak point with very high gain at the resonant frequency, resulting in significant performance degradation in disturbance rejection ability. In this case, a virtual term $z\beta\boldsymbol{B}^{-1}$ is introduced to reconstruct the PMSM model to improve the disturbance rejection capability. The feedback term is composed of three parts: one-step lead operator z, coefficient β and the constant $\boldsymbol{B}^{-1}$. In this way, the transfer function of the discrete-time PMSM model $G_{p3}(z)$ with feedback terms and its controller $G_{c3}(z)$ based on IMC principle can be presented as follows:

$$\begin{cases}G_{p3}(z)=\dfrac{i_{dq}(z)}{u_{dq}(z)}=\dfrac{\boldsymbol{B}T_s}{z\left[(z-1)\boldsymbol{I}-\boldsymbol{M}T_s+\beta T_s\boldsymbol{I}\right]}\\G_{c3}(z)=\delta\dfrac{\alpha T_s}{z(z-1)}G_{p3}^{-1}(z)\end{cases}. \tag{29}$$

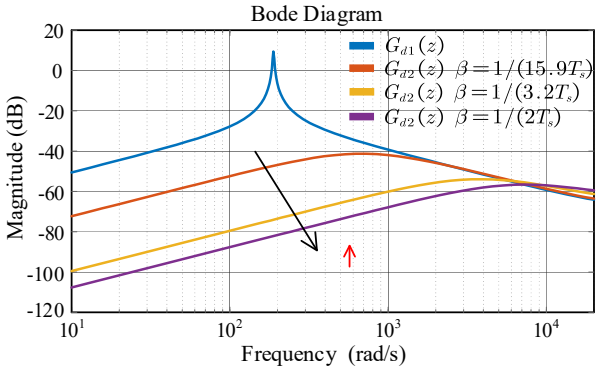

Fig. 3. Bode diagram of disturbance rejection ability with different value of β.

By reconstructing the virtual PMSM model, the disturbance rejection capability can be enhanced compared with the transfer function $G_{d1}(z)$, which is expressed as:

$$G_{d2}(z)=\frac{G_{p3}(z)}{1+zG_{p3}(z)G_{c3}(z)} =\frac{\boldsymbol{B}T_s(z-1)}{z\left((z-1)\boldsymbol{I}-\boldsymbol{M}T_s+\beta T_s\boldsymbol{I}\right)(z-1+\alpha T_s)}. \tag{30}$$

Fig. 3 illustrates the bode diagram which compares the disturbance rejection capability of the controller using (28) and (30). By introducing the active damping framework and adjusting the coefficient β, the disturbance rejection ability of the system can be greatly enhanced. It is noted that different from the extended state observer, β in the proposed structure only determines the disturbance rejection ability and does not affect the dynamic response of the current. Nevertheless, Since the two disturbance rejection transfer functions are different, the detailed performance will be verified in the experiment.

Based on the stability rule: the poles of the transfer function are located in a unit circle, limiting the range of β with $[0, T_s^{-1}]$. It should be noted that although increasing β can enhance the disturbance rejection ability at low and medium frequencies, the disturbance rejection capability at high frequencies could be reduced. Moreover, β should be selected considering the system noises in practical applications.

In order to reduce the computation burden, the voltage prediction can be implemented as follows:

$$\begin{cases} \boldsymbol{e}_{dq}(k)=\boldsymbol{i}_{dq}^{*}(k)-\boldsymbol{i}_{dq}(k+1) \\ \boldsymbol{P}_{dq}(k)=\alpha\delta\boldsymbol{B}^{-1}\boldsymbol{e}_{dq}(k) \\ \boldsymbol{Q}_{dq}(k)=\alpha\delta\boldsymbol{B}^{-1}(\beta T_s\boldsymbol{I}-\boldsymbol{M}T_s)\boldsymbol{e}_{dq}(k) \\ \boldsymbol{T}_{dq}(k)=\boldsymbol{Q}_{dq}(k-1)+\boldsymbol{T}_{dq}(k-1) \\ \boldsymbol{u}_{dq}^{*}(k)=\boldsymbol{P}_{dq}(k)+\boldsymbol{T}_{dq}(k)-\boldsymbol{D}-\boldsymbol{i}_{dq}(k+1)(\boldsymbol{B}^{-1}\beta-\boldsymbol{\Xi}). \end{cases} \tag{31}$$

Compared with conventional dead-beat prediction with (11), an extra integral term for disturbance rejection and a new coefficient for anti-parameter mismatch have been included in (31). Here, α is set as $1/T_s$ to achieve the dead-beat response. By setting β=0, and δ=1, (31) can be equivalent to (11).

C. Delay Compensation Using the Current Estimator

From (31), it is seen that the calculation of the reference voltage requires the predicted *dq*-axis current in (10) to compensate the controller delay. However, the accuracy of predicted current is prone to be affected by the parameter variation, which thereby degrades the control performance. In this case, a simple current predictor is developed to control the dynamic response of the current and lower the parameter sensitivity independently.

In order to obtain the predicted directly, the predicted current $z\tilde{\boldsymbol{i}}_{dq}(z)$ is considered as the output of the plant, last instant *dq*-axis voltage $z^{-1}\boldsymbol{u}_{dq}(z)$ and two feedback terms are considered as disturbance, and the distorted voltages caused by parameter mismatch $\boldsymbol{u}_{dqp}(z)$ are considered as input of the plant. Hence, the transfer function of the PMSM model with feedback terms $G_{pp}(z)$ in the current predictor can be derived as follows:

$$G_{pp}(z)=\frac{z\tilde{\boldsymbol{i}}_{dq}(z)}{z^{-1}\boldsymbol{u}_{dq}(z)}=\frac{\boldsymbol{B}T_s}{\boldsymbol{I}-z^{-1}\boldsymbol{I}-z^{-1}\boldsymbol{M}T_s+z^{-1}\beta T_s\boldsymbol{I}}. \tag{32}$$

Based on the IMC principle, the controller in the current predictor can be designed as

$$G_{cp}(z)=\frac{\sigma T_s z}{z-1}G_{pp}^{-1}(z), \tag{33}$$

where σ is the bandwidth of the current predictor. It should be noted that a larger σ can enhance the current dynamic response, while at the cost of a larger amount of noises. Compared to MPC using the ESO, the noises can be attenuated by tuning σ without influencing the disturbance rejection ability, while ESO can only adjust the observer bandwidth. Subsequently, σ should be selected based on the actual noise level.

The superposition theorem in this system includes both the disturbance closed-loop transfer function and the command tracking closed-loop transfer function, i.e. the sum of feedforward and disturbance paths. Hence, through the superposition principle, the current predictor output $z^{-1}\boldsymbol{u}_{dq}(z)$ can be obtained (the sum of the input signal effect and the disturbance signal effect) as follows:

$$\begin{aligned} z\tilde{\boldsymbol{i}}_{dq}(z)&=\boldsymbol{i}_{dq}(z)\cdot\frac{G_{cp}(z)G_{pp}(z)}{1+z^{-1}G_{cp}(z)G_{pp}(z)} \\ &\quad+\left[z^{-1}\boldsymbol{u}_{dq}(z)+\boldsymbol{i}_{dq}(z)(\boldsymbol{\Xi}+\beta\boldsymbol{B})\right]\cdot\frac{G_{pp}(z)}{1+z^{-1}G_{cp}(z)G_{pp}(z)} \\ &=\boldsymbol{i}_{dq}(z)+\frac{\left[z^{-1}\boldsymbol{u}_{dq}(z)+\boldsymbol{i}_{dq}(z)(\boldsymbol{\Xi}+\beta\boldsymbol{B})\right]\boldsymbol{B}T_s(1-z)}{\boldsymbol{I}-z^{-1}\boldsymbol{I}-z^{-1}\boldsymbol{M}T_s+z^{-1}\beta T_s\boldsymbol{I}}. \end{aligned} \tag{34}$$

The current estimation method can be implemented by replacing the predicted current calculated from (10) with $z\tilde{\boldsymbol{i}}_{dq}(z)$, and combining it with the feedback terms.

D. Implementation of the Control Algorithm

The block diagram of the proposed method is illustrated in Fig. 4. In summary, the control algorithm can be implemented by 5 key steps, as presented below:

Step 1: The one-step delay of measured current is compensated using the current estimator.

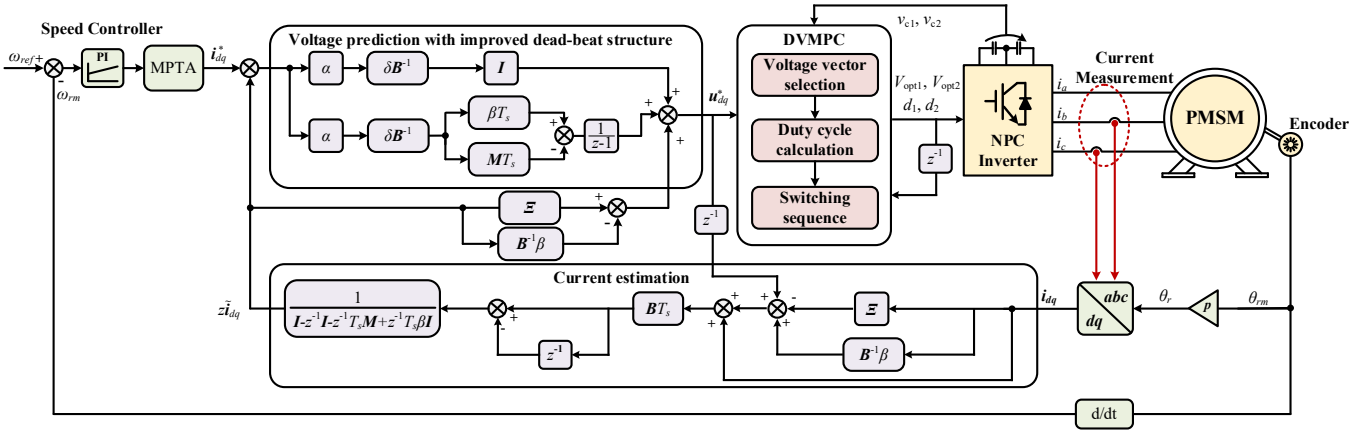

Fig. 4. Block diagram of the proposed method.

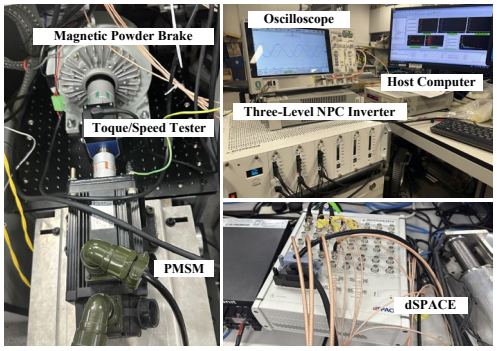

Fig. 5. Experimental setup used for verification.

TABLE II. Parameters of the control system in experiment

Parameters	Value	Unit
Rated power (P_N)	1.5	*kW*
Rated current (I_N)	7	A
Rated Speed (N_r)	2000	r/min
Pole pairs (p)	4	N/A
Stator resistance (R_s)	0.65	*Ω*
d-axis inductance (L_d)	1.95	*mH*
q-axis inductance (L_q)	1.95	*mH*
PM flux (ψ_f)	0.135	*Wb*
Sampling time (T_s)	100	*μs*

Step 2: The reference voltage is computed using (30), based on the reference current and the estimated current.

Step 3: Two optimal voltage vectors are selected via the exhaustive search of the cost function.

Step 4: The optimal duty cycle of the two active voltage vectors is calculated.

Step 5: The small voltage vector type is determined for NP balancing, followed by switching sequence adjustment and pulse generation.

VI. Experimental Demonstration

The effectiveness and superiority of the proposed DV-MPC is demonstrated on the platform depicted in Fig. 5. The parameters of the control system are summarized in TABLE II.

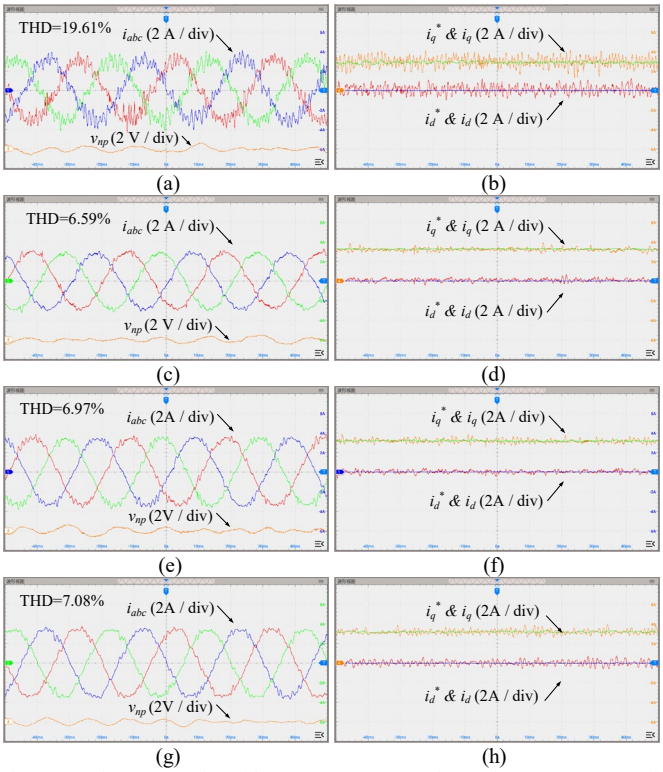

Fig. 6. Steady state results with 500 rpm rotor speed. (a), (b) SV-MPC. (c), (d) DV-MPC-I. (e), (f) DV-MPC-II. (g), (h) DV-MPC-III.

The dSPACE MircroLabBox has served as the controller for the PMSM powered by a three-level NPC inverter, and the load torque is implemented with a magnetic powder brake. To comprehensively evaluate performance of the proposed method (DV-MPC-III), the conventional single vector MPC (SV-MPC), the DV-MPC (DV-MPC-I), and the DV-MPC with ESO (DV-MPC-II) have been compared in this section. To achieve same dynamic response and make a fair comparison, both the observer bandwidth of DV-MPC-II the coefficients β in DV-MPC-III are set as $0.1/T_s$ (159 Hz), which can well balance the tradeoff between the disturbance rejection capability and the measurement noise suppression. α in DV-MPC-III is set as $1/T_s$ (1591 Hz), which is the same as the dead-beat approach.

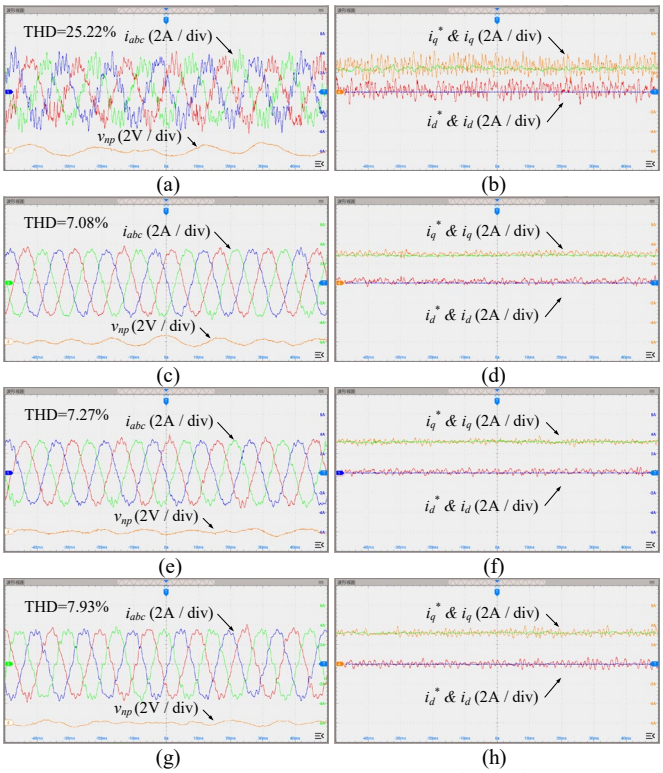

Fig. 7. Steady state results with 1000 rpm rotor speed. (a), (b) SV-MPC. (c), (d) DV-MPC-I. (e), (f) DV-MPC-II. (g), (h) DV-MPC-III.

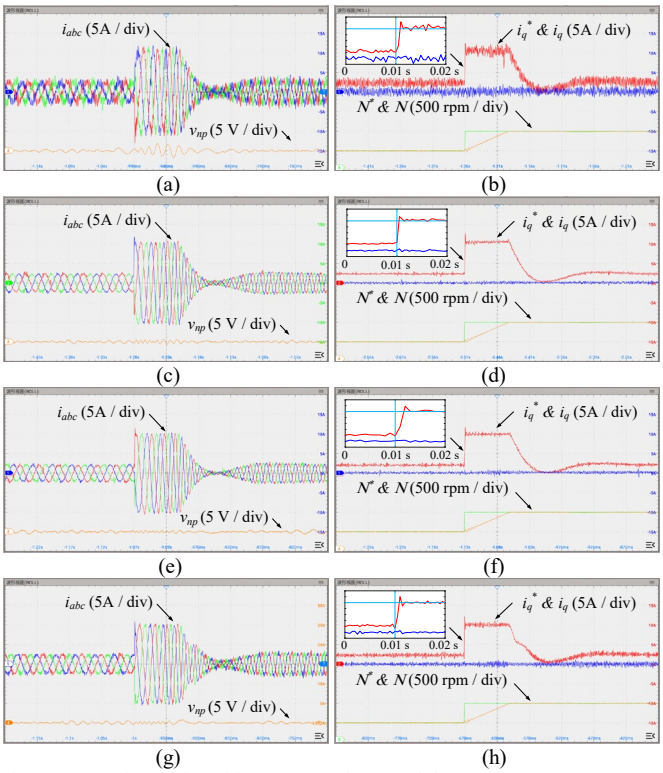

Fig. 8. Dynamic results with rotor speed stepped from 500 to 1000 rpm. (a), (b) SV-MPC. (c), (d) DV-MPC-I. (e), (f) DV-MPC-II. (g), (h) DV-MPC-III.

TABLE III. Execution time of different MPC methods

Methods	Turnaround time	ADC	Pulse Generation
SV-MPC	21.2 µs	6.3 µs	7.7 µs
DV-MPC-I	25.4 µs		
DV-MPC-II	25.7 µs		
DV-MPC-III	25.9 µs		

A. Steady State Performance

This part evaluates the steady state performance in different rotor speed conditions. In Fig. 6 and Fig. 7, the PMSM operates in the steady state with 2.5 Nm load torque, while the rotor speed is set as 500 rpm and 1000 rpm, respectively. All method can well maintain the NP potential around 0. Compared with the conventional SV-MPC, DV-MPC can significantly reduce the *dq* current ripples, and the current harmonic distortion can be decreased by approximate 65% in this case, demonstrating the effectiveness of the double vector algorithm. Meanwhile, it is observed that DV-MPC-II and the proposed DV-MPC-III can exhibit similar steady state performance, but have a bit higher current THD compared to DV-MPC-I when no or very subtle parameter mismatch occurs. This is caused by the noises induced by the observer and active damping.

In addition, comparing DV-MPC-I, DV-MPC-II and DV-MPC-III, a subtle current tracking offset exists in DV-MPC-I, because of the slight variation of the nominal parameters. This slight offset can be well compensated in DV-MPC-II and proposed DV-MPC-III.

B. Execution Time Evaluation

The execution times of four MPC methods on the dSPACE controller were evaluated, as summarized in TABLE III. The turnaround time for the SV-MPC method is 21.2 µs, whereas the DV-MPC methods exhibit an increase of approximately 4 µs due to the additional computation required for the second voltage vector and its corresponding duty cycle. Notably, the proposed DV-MPC-III method introduces only a slight increase in computational cost, which is negligible when compared to the DV-MPC-I and DV-MPC-II methods.

C. Dynamic Performance

In this part, the dynamic performance with respect to the reference speed step scenario has been evaluated, as shown in Fig. 8. Herein, the reference speed steps from 500 to 1000 rpm, and the load torque is kept constant during this transient. DV-MPC methods have less NP voltage oscillation during this transient compared to SV-MPC method, since the NP balance is achieved during each control cycle. From the zoom view of the *dq* currents, it shows that DV-MPC-II presents a little bit slower current rising response due to the low observer response. As a contrast, by setting $\alpha = 1/T_s$, the proposed DV-MPC-III can achieve the same current responses as DV-MPC-I and SV-MPC, which demonstrates that the fast dead-beat response using the conventional dead-beat voltage prediction can be also achieved by the proposed DV-MPC-III method.

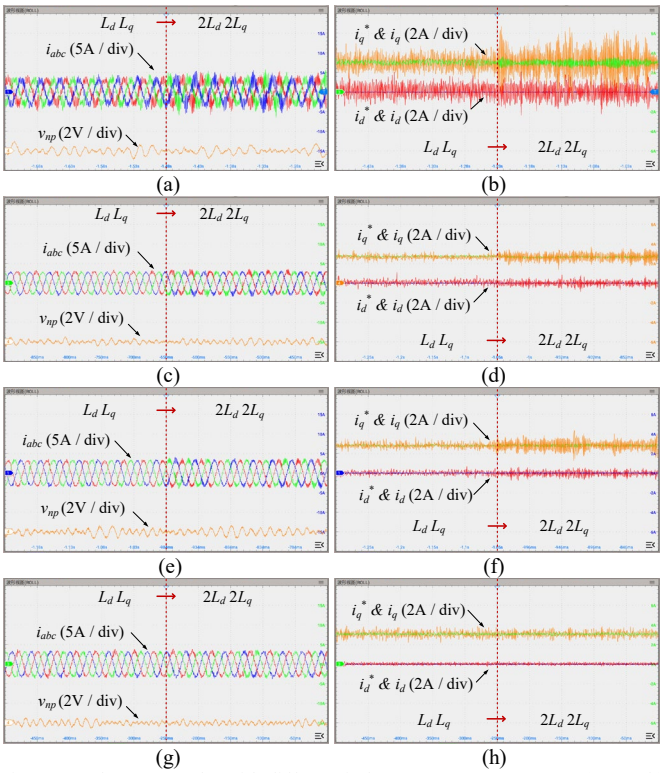

Fig. 9. Steady state results with different inductance (L_d, L_q to $2L_d$, $2L_q$). (a), (b) SV-MPC. (c), (d) DV-MPC-I. (e), (f) DV-MPC-II. (g), (h) DV-MPC-III.

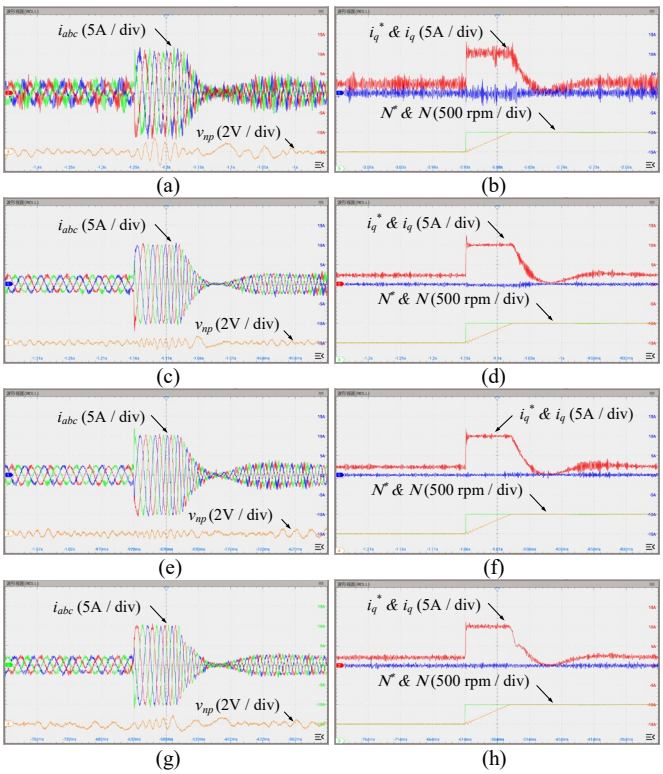

Fig. 10. Dynamic results under parameters mismatch ($0.5R_s$, $2L_d$ and $2L_q$) with rotor speed stepped from 500 to 1000 rpm. (a), (b) SV-MPC. (c), (d) DV-MPC-I. (e), (f) DV-MPC-II. (g), (h) DV-MPC-III.

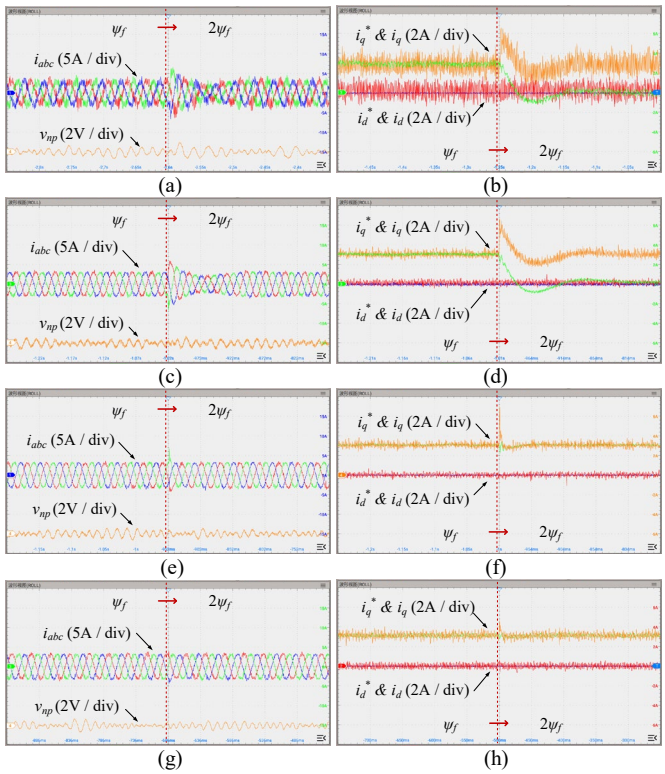

Fig. 11. Disturbance rejection test results with the flux linkage sudden change from ψ_f to $2\psi_f$. (a), (b) SV-MPC. (c), (d) DV-MPC-I. (e), (f) DV-MPC-II. (g), (h) DV-MPC-III.

D. Robustness Performance

The robustness of the proposed method against parameter mismatch is evaluated in this part. To this end, the steady state performance, dynamic performance under parameter mismatch and disturbance rejection performance is tested. In Fig. 9, the PMSM operates in 500 rpm while the *dq* inductances of the controller are suddenly changed from their nominal values to the double time nominal values. It is observed that SV-MPC and DV-MPC-I are very sensitive to the variation of inductance value. As a comparison, DV-MPC-II can present better performance due to the adopted ESO, but the current ripple induced by parameter mismatch cannot be fully compensated. For the proposed DV-MPC-III, the variation of inductance can be well compensated, which thereby exhibits very strong parameter robustness in the test results.

To further compare the robust performance of the proposed method, Fig. 10 presents the dynamic performance with reference speed step under severe parameters mismatch, wherein the control parameters are set as $0.5R_s$, $2L_d$ and $2L_q$, respectively. From the comparison, it can be seen that considerable current oscillation occurs with SV-MPC, DV-MPC-I and DV-MPC-II, especially when the *dq* current is recovering to the steady state. While for the proposed DV-MPC-II, the dynamic performance is not distinctively deteriorated under the multiple parameters mismatch condition.

The disturbance rejection ability is a critical factor in evaluating the proposed method. Hence, the performances of the external disturbance rejection with the four control methods are evaluated in this part, which is illustrated in Fig. 11. Herein,

the disturbance is implemented by a sudden change of the flux linkage ψ_f to its double time nominal value in the controller. Since the disturbance rejection is not considered, significant disturbances during the transient and a large current tracking offsets can be observed for SV-MPC and DV-MPC-I. By including the ESO, DV-MPC-II achieves good disturbance rejection ability and well compensates the current offsets compared with the conventional methods. For proposed DV-MPC-III, transient current oscillations are prominently attenuated compared to other methods, demonstrating superior disturbance rejection performance over DV-MPC-II with the same bandwidth. Furthermore, current offsets are completely eliminated with DV-MPC-III after recovering to the steady state.

VII. Conclusion

This paper presents a double-vector model predictive control method with enhanced robustness and disturbance rejection capabilities for three-level inverter-fed PMSM drives. The proposed method employs a simplified voltage tracking cost function based on a dead-beat approach, combined with double-vector synthesis to reduce computational burden while improving current tracking performance. An enhanced dead-beat structure, incorporating three tunable coefficients, is introduced to integrate active damping and provide an additional degree of freedom. By setting $\alpha = 1/T_s$, a dead-beat response is achieved, while systematic tunning of β and δ enables improved disturbance rejection and parametric robustness. Experimental results validate the effectiveness of the proposed method, demonstrating its ability to operate under parameter mismatch and external disturbances, which may not be possible with conventional dead-beat MPC. The proposed control method overall may be very useful for practical industrial AC machine drives, considering some severe and complex operation environments.

References

[1] E. Sayed et al., "Review of electric machines in more-/hybrid-/turbo-electric aircraft," *IEEE Trans. Transp. Electrific.*, vol. 7, no. 4, pp. 2976–3005, Dec. 2021.

[2] W. Cao, S. Member, B. C. Mecrow, G. J. Atkinson, J. W. Bennett, and D. J. Atkinson, "Overview of electric motor technologies used for more electric aircraft (MEA)," *IEEE Trans. Ind. Electron.*, vol. 59, no. 9, pp. 3523–3531, Sep. 2012.

[3] F. Guo, Z. Ma, F. Diao, Y. Zhao, and P. Wheeler, "Hybrid virtual coordinate-driven CBPWM strategy of three-level T-type NPC converters for electric aircraft propulsion applications," *IEEE Trans. Ind. Electron.*, vol. 71, no. 3, pp. 2309–2319, Mar. 2024.

[4] D. Zhang, J. He, and D. Pan, "A megawatt-scale medium-voltage high-efficiency high power density 'SiC+Si' hybrid three-level ANPC Inverter for aircraft hybrid-electric propulsion systems," *IEEE Trans. Ind. Appl.*, vol. 55, no. 6, pp. 5971–5980, Nov.-Dec. 2019.

[5] C. Liu, K. T. Chau, C. H. T. Lee and Z. Song, "A critical review of advanced electric machines and control strategies for electric vehicles," *Proc. IEEE*, vol. 109, no. 6, pp. 1004-1028, Jun. 2021.

[6] J. A. Suul, K. Ljokelsoy, T. Midtsund and T. Undeland, "Synchronous reference frame hysteresis current control for grid converter applications," *IEEE Trans. Ind. Appl.*, vol. 47, no. 5, pp. 2183-2194, Sep.-Oct. 2011.

[7] A. Dey, P. P. Rajeevan, R. Ramchand, K. Mathew and K. Gopakumar, "A space-vector-based hysteresis current controller for a general n-level inverter-fed drive with nearly constant switching frequency control," *IEEE Trans. Ind. Electron.*, vol. 60, no. 5, pp. 1989-1998, May 2013

[8] L. Harnefors and H. -P. Nee, "Model-based current control of AC machines using the internal model control method," *IEEE Trans. Ind. Appl.*, vol. 34, no. 1, pp. 133-141, Jan.-Feb. 1998.

[9] X. Zhang, B. Hou and Y. Mei, "Deadbeat predictive current control of permanent-magnet synchronous motors with stator current and disturbance observer," *IEEE Trans. Power Electron.*, vol. 32, no. 5, pp. 3818-3834, May 2017.

[10] S. Li and Z. Liu, "Adaptive speed control for permanent-magnet synchronous motor system with variations of load inertia," *IEEE Trans. Power Electron.*, vol. 56, no. 8, pp. 3050-3059, Aug. 2009.

[11] S. Vazquez, J. Rodriguez, M. Rivera, L. G. Franquelo and M. Norambuena, "Model predictive control for power converters and drives: advances and trends," *IEEE Trans. Ind. Electron.*, vol. 64, no. 2, pp. 935–947, Feb. 2017.

[12] J. Rodriguez, C. Garcia, A. Mora *et al.*, "Latest advances of model predictive control in electrical drives. Part I: basic concepts and advanced strategies," *IEEE Trans. Power Electron.*, vol. 37, no. 4, pp. 3927-3942, Apr. 2022.

[13] F. Wang, Y. Wei, H. Young, D. Ke, H. Xie, and J. Rodriguez, "Continuous-control-set model-free predictive fundamental current control for PMSM system," *IEEE Trans. Power Electron.*, vol. 38, no. 5, pp. 1–11, Mar. 2023.

[14] P. Karamanakos and T. Geyer, "Guidelines for the design of finite control set model predictive controllers," *IEEE Trans. Power Electron.*, vol. 35, no. 7, pp. 7434–7450, Jul. 2020.

[15] X. Zhang, Y. Cao, C. Zhang and S. Niu, "Model predictive control for PMSM based on the elimination of current prediction errors," *IEEE J. Emerg. Sel. Top. Power Electron.* vol. 12, no. 3, pp. 2651-2660, Jun. 2024.

[16] C. Xue, D. Zhou, and Y. Li, "Finite-control-set model predictive control for three-level NPC inverter-fed PMSM drives with LC filter," *IEEE Trans. Ind. Electron.*, vol. 68, no. 12, pp. 11980–11991, Dec. 2021.

[17] X. Tang, S. Niu, K. T. Chau, X. Yuan, and W. L. Chan, "Model predictive control of three-level NPC inverter-fed PMSM drives based on a novel vector-selection scheme," *IEEE J. Emerg. Sel. Top. Power Electron.*, early access: 10.1109/JESTPE.2024.3520912.

[18] Z. Sun, S. Xu, G. Ren, C. Yao, G. Ma and J. Jatskevich, "Weighting-factor-less model predictive control with multi objectives for three-level hybrid ANPC inverter drives," *IEEE J. Emerg. Sel. Top. Power Electron.*, vol. 11, no. 5, pp. 4726-4738, Oct. 2023.

[19] T. Geyer and D. E. Quevedo, "Performance of multistep finite control set model predictive control for power electronics," *IEEE Trans. Power Electron.*, vol. 30, no. 3, pp. 1633–1644, Dec. 2014.

[20] J. Holtz, "Predictive finite-state control — when to use and when not," *IEEE Trans. Power Electron.*, vol. 37, no. 4, pp. 4225–4232, Apr. 2022.

[21] Y. Zhang, D. Xu, and L. Huang, "Generalized multiple-vector-based model predictive control for PMSM drives," *IEEE Trans. Ind. Electron.*, vol. 65, no. 12, pp. 9356–9366, Dec, 2018.

[22] C. Hu *et al.*, "A novel double-voltage-vector model-free predictive current control method for two-level voltage source inverters," *IEEE Trans. Ind. Electron.*, vol. 70, no. 6, pp. 5872–5884, Jun. 2023.

[23] D. Zhou, Z. Quan, and Y. Li, "Hybrid model predictive control of ANPC converters with decoupled low-frequency and high-frequency cells," *IEEE Trans. Power Electron.*, vol. 35, no. 8, pp. 8569–8580, Aug. 2020.

[24] Y. Yang, H. Wen, R. Chen, *et al.*, "An efficient model predictive control using virtual voltage vectors for three-phase three-level converters with constant switching frequency," *IEEE Trans. Ind. Electron.*, vol. 69, no. 4, pp. 3998–4009, Apr. 2022.

[25] Y. Liu, S. Huang, W. Liao, *et al.*, "Three-vector-based model predictive torque control for dual three-phase PMSM with torque and flux ripples reduction," *IEEE Trans. Power Electron.*, vol. 39, no. 8, pp. 10009–10020, Aug. 2024.

[26] Y. Wang, X Wang, W. Xie, F. Wang, *et al.*, "Deadbeat model-predictive torque control with discrete space-vector modulation for PMSM drives," *IEEE Trans. Ind. Electron.*, vol. 64, no. 5, pp. 3537–3547, May 2017.

[27] X. Zhang and B. Hou, "Double vectors model predictive torque control without weighting factor based on voltage tracking error," *IEEE Trans. Power Electron.*, vol. 33, no. 3, pp. 2368–2380, Mar. 2018.

[28] Q. Wang, Haitao Yu, Chen Li, *et al.*, "A low-complexity optimal switching time-modulated model-predictive control for PMSM with three-level NPC converter," *IEEE Trans. Transp. Electrif.*, vol. 6, no. 3, pp. 1188–1198, Sep. 2020.

[29] T. Liu, A. Chen, C. Qin, J. Chen, and X. Li, "Double vector model predictive control to reduce common-mode voltage without weighting factors for three-level inverters," *IEEE Trans. Ind. Electron.*, vol. 67, no. 10, pp. 8980–8990, Oct. 2020.

[30] Y. Wang, Y. Yang, S, Chen, *et al.*, "An improved model predictive voltage control with reduced computational burden for T-type three-phase three-level inverters," *IEEE Trans. Power Electron.*, vol. 39, no. 2, pp. 2115–2127, Feb. 2024.

[31] X. Yuan, S. Zhang, and C. Zhang, "Improved model predictive current control for SPMSM drives with parameter mismatch," *IEEE Trans. Ind. Electron.*, vol. 67, no. 2, pp. 852–862, Feb. 2020.

[32] S. Zhu, W. Huang, Y. Yan and Z. Niu, "High-damped complex vector current regulator for PMSM based on active damping function," *IEEE Trans. Ind. Electron.*, vol. 38, no. 4, pp. 5204-5216, Apr. 2023.

[33] J. Wen, X. Yuan, S. Niu, and W. L. Chan, "A robust complex vector PI current controller with deadbeat response for PMSM drives," *IEEE Trans. Ind. Electron.*, vol. 72, no. 5, pp. 4671-4681, May 2025.

[34] F. Wang, D. Ke, X. Yu, and D. Huang, "Enhanced predictive model based deadbeat control for PMSM drives using exponential extended state observer," *IEEE Trans. Ind. Electron.*, vol. 69, no. 3, pp. 2357–2369, Mar. 2022.

[35] X. Yuan, Y. Zuo, Y. Fan, and C. H. T. Lee, "Model-free predictive current control of SPMSM drives using extended state observer," *IEEE Trans. Ind. Electron.*, vol. 69, no. 7, pp. 6540–6550, Jul. 2022.

[36] F. Wang, W. Kong, and R. Qu, "Model parameter self-correcting deadbeat predictive current control for SPMSM drives," *IEEE Trans. Ind. Electron.*, vol. 72, no. 3, pp. 2357–2368, Mar. 2025.

[37] M. Yang, S. Huang, W. Liao, *et al.*, "Nonparametric predictive current control for SPMSM with adaptive cascade extended noise state observer," *IEEE Trans. Power Electron.*, vol. 40, no. 1, pp. 1717–1727, Jan. 2025.

Zhenyao Sun received the B.Sc. and M.Sc. degrees in Vehicle Engineering from Beijing Forestry University, Beijing, China, and Xihua University, Chengdu, China, in 2015 and 2019, respectively, and the Ph.D. degree in Vehicle Application Engineering from Southwest Jiaotong University, Chengdu, China, in 2024.

From 2022 to 2023, he was a Joint Ph.D. student at The University of British Columbia, Vancouver, BC, Canada. Since 2024, he has been a Postdoctoral Fellow at The Hong Kong Polytechnic University, Hong Kong. His research focuses on advanced control strategies for multilevel power converters and electric motor drives.

Junkai Wen received the B.Eng. degree in electrical engineering and automation from Shanghai Ocean University, Shanghai, China, in 2021, and the M.Sc. degree in electrical power system with distinction from the University of Birmingham, Birmingham, U.K., in 2022. He is currently working toward the Ph.D. degree in electrical engineering with the Department of Electrical and Electronic Engineering, The Hong Kong Polytechnic University, Hong Kong, China.

His research interests include ac motor drives and power electronics.

Xin Yuan (Senior Member, IEEE) received the B.Sc. degree in electrical engineering and automation from Beijing Union University, Beijing, China, in 2013, and the M.Phil. degree from the North China University of Technology, Beijing, in 2016, and the Ph.D. degree from Beijing Institute of Technology, Beijing, in 2020, both in electrical engineering. He joined as a Lecturer (Assistant Professor) with the School of Engineering, The University of Aberdeen, Aberdeen, U.K., in 2024. Before joining The University of Aberdeen, he worked as a Research Assistant Professor with the Department of Electrical and Electronic Engineering, The Hong Kong Polytechnic University, Hong Kong, China, and as a Research Associate with the PEMC Group, University of Nottingham, Nottingham, U.K. In 2020, he was also a Postdoctoral Research Fellow with the School of Electrical and Electronic Engineering, Nanyang Technological University, Singapore.

Guangtong Ma (Member, IEEE) received the B.E. and Ph.D. degrees in electrical engineering from Southwest Jiaotong University (SWJTU), Chengdu, China, in 2005 and 2009, respectively.

From 2011 to 2013, he was an Alexander von Humboldt Research Fellow with Technische Universität Darmstadt, Darmstadt, Germany. Since 2010, he has been with the State Key Laboratory of Rail Transit Vehicle System, SWJTU, where he is currently a full professor and deputy director. Since 2024, he has also been a Dean with the School of Electrical Engineering, SWJTU. His research interests include superconducting levitation, linear motor and traction motor.

Shuangxia Niu (Senior Member, IEEE) received the B.Sc. and M.Sc. degrees from Tianjin University, Tianjin, China, in 2002 and 2005, respectively, and the Ph.D. degree from the University of Hong Kong, Hong Kong, SAR, China, in 2009, all in electrical engineering. Currently, she is a Professor with the Department of Electrical and Electronic Engineering, The Hong Kong Polytechnic University, Hong Kong, China.

She authored or coauthored more than 200 papers in leading journals. Prof. Niu is currently an Associate Editor for IEEE Transaction on Industrial Electronics and IEEE Journal of Emerging and Selected Topics in Power Electronics. She is a Distinguished Lecturer of IEEE Vehicular Technology Society.

K. T. Chau (Fellow, IEEE) received the B.Sc. (Eng.), M.Phil., and Ph.D. degrees in electrical and electronic engineering from The University of Hong Kong, Hong Kong, in 1988, 1991, and 1993, respectively. Currently, he serves as Chair Professor of Electrical Energy Engineering at the Research Centre for Electric Vehicles and Department of Electrical and Electronic Engineering, The Hong Kong Polytechnic University. His research interests include electric and hybrid vehicles, power electronics and drives, and renewable energies. He is the author of nine books and more than 350 journal papers.

Prof. Chau is a Fellow of the Institution of Engineering and Technology (IET), U.K., and of the Hong Kong Institution of Engineers. He is also a Co-editor of the Journal of Asian Electric Vehicles. He is a Chartered Engineer. He was the recipient of the Changjiang Chair Professorship from the Ministry of Education, China, and the Environmental Excellence in Transportation Award for Education, Training, and Public Awareness from the Society of Automotive Engineers International.